

Selective Frequency Conversion With Coupled Time-Modulated Cavities

Galaad Altares Menendez* and Bjorn Maes

*Micro- and Nanophotonic Materials Group, Research Institute for Materials Science and Engineering,
University of Mons, 20 Place du Parc, B-7000 Mons, Belgium*

(Dated: July 8, 2019)

Time dependence in photonic structures leads to a number of intriguing and useful phenomena such as optical isolation, topological states of light and frequency conversion. Here we present a mechanism to achieve efficient and selective frequency conversion using a system of two time-modulated cavities. This setup allows to fine-tune the conversion process by controlling important parameters such as the inter-cavity coupling and the external excitation frequency. Both symmetric and asymmetric (up- or down-conversion) outputs can be targeted at will. We describe the processes extensively, with for example a leading role for the dynamic modes of the coupled system, the Floquet modes.

I. INTRODUCTION

Temporal or dynamic modulation in photonic structures has been a topic of increasing interest, as it can induce unique optical functions. For example, time modulation can break reciprocity in various devices^{1,2}, leading to optical isolation without magnetic materials^{3,4}. This isolation mechanism is quite general, and can be applied to various contexts such as acoustics⁵, graphene plasmonics⁶ and so on. Furthermore, dynamic modulation can achieve frequency conversion without resorting to traditional nonlinear effects⁷⁻¹⁰. Recently, there are various developments to exploit the novel physical effects related to temporal symmetry breaking, for example to produce effective magnetic fields^{11,12}, to implement topological states of light^{13,14} or for time crystals¹⁵⁻¹⁷.

These time modulation effects are aided by photonic confinement, such as in high-index contrast cavities^{18,19}. Therefore, subwavelength confined plasmonic resonances can also be exploited, achieving e.g. efficient frequency conversion²⁰. In this setting, graphene can be highlighted as an interesting platform for tailorable plasmonics²¹⁻²⁴, since its conductivity can be effectively tuned^{25,26}, leading to time-modulated plasmonic modes in graphene structures.

Ginis et al. examined the possibility to produce a frequency comb by modulating the conductivity of a planar graphene sheet²⁷. However, the efficiency of this process is hampered because of the large change in conductivity needed to obtain a significant modulation in the transmission. In previous work we presented a way to overcome this limitation using a graphene ribbon array²⁸, with interaction between a single time-modulated resonance and the incident light. A plasmonic resonance in such an array allows to produce combs with a greatly enhanced efficiency, and with a fairly good control²⁹. Typically, frequency comb generation is implemented by four-wave mixing³⁰, with effective implementation in micro-ring resonators for example³¹.

In this work we extend the system to two time-modulated coupled resonances, instead of a single one. Importantly, this system turns out to be effective for *selective* frequency conversion, so that instead of an ex-

tensive frequency comb, we are targeting conversion towards specific frequencies, by exploiting the interference processes in play. The mechanism and our description are quite general, so that in practice various dielectric or plasmonic implementations, such as graphene ribbons with different widths, can be considered.

We mainly optimize the asymmetric conversion towards a single sideband, and the symmetric conversion towards two equally spaced sidebands. We consider the specific degenerate case first (when the two cavity resonance frequencies are equal), and then compare with the more general non-degenerate case. We elucidate the crucial role of the intermodal coupling constant and the source frequency, using various semi-analytical approaches. It is very interesting that the so-called ‘Floquet modes’ play an important role in these processes. We determine the band structure of these modes of the dynamic system, and observe for example that the conversion efficiency is greatly enhanced in the neighborhood of Floquet band anti-crossings.

We study the system using the well-established Coupled Mode Theory (CMT) equations for coupled cavities³²⁻³⁴. We employ this method with time-dependent resonance frequencies in Sec. II. We show that this system supports Floquet modes in Sec. III, and provide a method to obtain their frequencies. We then discuss how to achieve selective frequency conversion in Sec. IV, with an extensive evaluation of the process efficiency. In addition, Sec. V explains how a simple three-frequency analysis can determine the system parameters to achieve the desired conversion. Finally, in Sec. VI we derive an analytic approximation of the band structure of the Floquet modes using a perturbation analysis.

II. SETUP AND COUPLED MODE THEORY

We study a system of two coupled resonances, which can be created for example by two nearby cavities. Here, the resonance frequency of one of the cavities will be time-modulated, leading to the generation of new frequency components. A sketch of the system is depicted in Fig. 1(a). A possible way to physically implement this

setup could consist of two graphene ribbon arrays with different widths^{35,36} (Fig. 1(b)), as the conductivity can be dynamically modulated³⁷ in graphene.

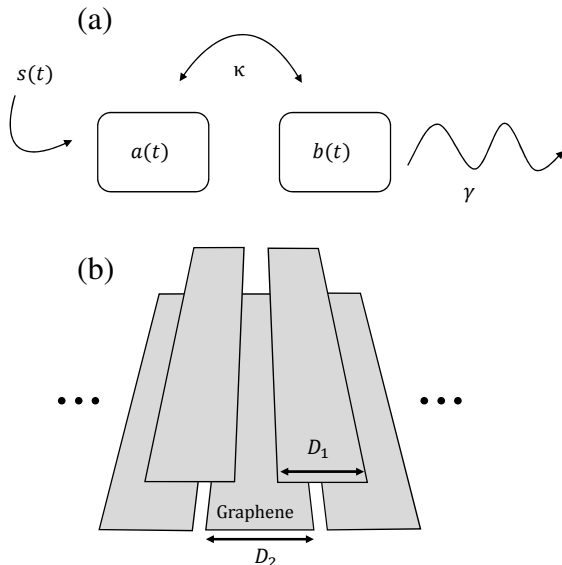


FIG. 1. (a) Representation of the system of coupled resonances. (b) Possible implementation using two coupled arrays of graphene ribbons. Each cavity corresponds to a plasmonic resonance in the graphene array, where different ribbon widths (D_1 and D_2) provide different resonance frequencies. The ribbons are repeated in the horizontal direction creating two vertically offset gratings.

To limit the number of parameters, we consider direct injection (amplitude $s(t)$) into one of the modes, which does not radiate (the so-called dark mode, amplitude $a(t)$), whereas the other mode (the bright one, $b(t)$) radiates, providing the output. We describe this two-cavity setup by a system of coupled equations with CMT³⁴:

$$\frac{da(t)}{dt} = i\omega_1 a(t) + i\kappa b(t) + s(t) \quad (1)$$

$$\frac{db(t)}{dt} = i\omega_2 b(t) + i\kappa a(t) - \gamma b(t) \quad (2)$$

where $a(t)$ and $b(t)$ are respectively the dark and bright mode amplitudes, γ is the outcoupling coefficient, κ is the coupling coefficient between the two cavities, $\omega_{1,2}$ are the (potentially time modulated) resonance frequencies, and $s(t)$ is the input, for which we use a nearly monochromatic gaussian pulse (with central frequency ω_0).

Here the source $s(t)$ can be considered as a dipolar emitter coupling to the field of the dark mode $a(t)$, in the weak-coupling limit. For systems with one or more input waveguides the model can be extended to take external interferences with reflection and transmission into account.

In this model the κ values are real so energy conservation is ensured. In order to get realistic parameter values

for the CMT model, we ran Finite-Element Method simulations of a graphene ribbon array²⁸. This allowed us to connect the CMT parameters to the physical properties of graphene arrays. We determined that the plasmon absorption rate in a typical setting can be one order of magnitude smaller than the plasmon outcoupling time, so for simplicity we do not consider these losses in this model.

Usually the resonant frequencies are constants, but here for time-modulation they become functions of time, and we will consider a periodic modulation. In this paper we focus on the case where only the bright mode resonance is modulated:

$$\omega_2(t) = \omega_2 + \delta \sin(\Omega t) \quad (3)$$

with ω_2 the ‘static’ resonance frequency, δ the modulation amplitude and Ω the modulation frequency. The modulation amplitudes δ we consider here are of the same order of magnitude as Ω . This modulation amplitude can be achieved with modest E_F changes²⁸, because resonance frequencies in graphene ribbons strongly depend on E_F and because we consider modulation frequencies such that $\omega_{1,2} \gg \Omega$. The phenomena are similar if we modulate the other mode, or if we modulate both modes. Other modulation functions³⁸, such as step-functions or shocks^{39,40}, could also be considered in future work.

This work is distinct from the effects in most modulators: Typically, the modulation frequency is slow and the modulation amplitude is not too high compared to the outcoupling rate²⁹. In those cases (the adiabatic limit), the approximation of a time-dependent transmission, neglecting the interaction with the cavity modulation, is often used. However, here the time-dependence is non-trivial, and the light stays trapped in the cavity for a few modulation cycles. In this high-frequency limit, new frequencies are generated and the parameters governing this frequency conversion are investigated in detail further on.

In previous work²⁸, with a single-cavity system that is time modulated, it was observed that one obtains a wide frequency comb, with components separated by the modulation frequency Ω . While that setup is useful for generating a wide range of new frequencies, it is more difficult to obtain an efficient conversion to a specific frequency. With the two-cavity setup described here, it becomes possible to obtain more focused features, such as selective frequency conversion.

III. FLOQUET MODES

In this section we introduce Floquet modes, as they play an important role to understand and optimize the frequency conversion process further on. Floquet modes are the time analogues of Bloch modes in space, with a time-periodic modulation of the index, instead of a space-periodic index distribution for Bloch modes. In our setup

the optical potential (via the resonance frequency $\omega_2(t)$) is periodic in time so the Floquet modes can be defined.

The static non-driven coupled system (i.e. constant frequencies $\omega_{1,2}$) has two modes with frequencies $\omega_{\pm} = \frac{\omega_1 + \omega_2}{2} \pm \frac{1}{2}\sqrt{(\omega_1 - \omega_2)^2 + 4\kappa^2}$. In the degenerate case where $\omega_1 = \omega_2 = \omega_{1,2}$, the two mode frequencies take the simple form $\omega_{\pm} = \omega_{1,2} \pm \kappa$ (see red dashed lines in Fig. 2).

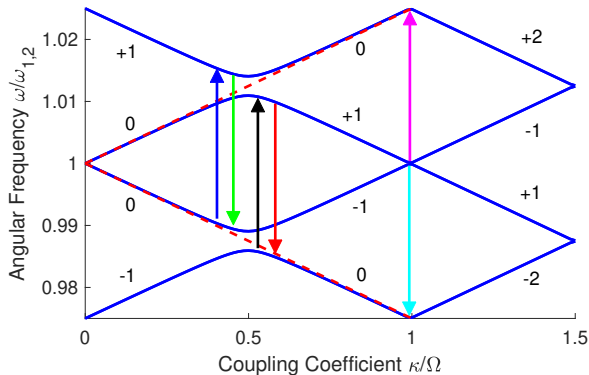


FIG. 2. Blue lines: Floquet modes of the system for the degenerate case, where $\omega_{1,2} = 2\pi \times 10^{13}$ rad/s, $\Omega = 2\pi \times 2.5 \times 10^{11}$ rad/s and $\delta = \Omega/2$. Dashed red lines: static resonance frequencies for the degenerate case ($\omega_{\pm} = \omega_{1,2} \pm \kappa$). The four arrows near $\kappa = \Omega/2$ represent the transitions of interest that we study in Sec. IV A while the two arrows near $\kappa = \Omega$ represent the transitions that we study in Sec. IV B. An anti-crossing appears at $\kappa = \Omega/2$ where the static modes intersect.

With the introduction of time modulation, these frequencies are adjusted, and have multiple Floquet mode branches with frequency difference Ω (see blue solid lines in Fig. 2). Interestingly, when these branches meet as a function of κ they can lead to anti-crossings (see around $\kappa = \Omega/2$ in Fig. 2). This is a different effect than bandgaps that appear for propagative Floquet modes⁴¹. Here we study two coupled localized resonances so no true bandgap is opened.

One way to compute the Floquet mode frequencies is to write Eqs 1 and 2 (without the source term) in matrix form⁴²:

$$-i \frac{dF(t)}{dt} = H(t)F(t) \quad (4)$$

where $F(t)$ is a matrix of eigenvectors and $H(t)$ is the time-modulated Hamiltonian. Floquet's theorem insures that a solution exists in the form

$$F(t) = \Phi(t)e^{iQt} \quad (5)$$

where $\Phi(t)$ is a matrix of periodic functions and Q is a constant diagonal matrix containing the Floquet eigenvalues (compare with the typical Bloch mode form). Since $\Phi(t)$ and $H(t)$ are matrices of periodic functions,

it is convenient to expand them in Fourier series:

$$F_{ab}(t) = \sum_n F_{ab}^n e^{in\Omega t} e^{iq_b t} \quad (6)$$

$$H_{ab}(t) = \sum_n H_{ab}^n e^{in\Omega t} \quad (7)$$

where q_b are the diagonal elements of Q , $\Omega = 2\pi/T$, and T is the period of $\Phi(t)$ (see Eq. 3). The indices a and b denote a cavity mode, while index n (and also m in the following equations) represents Fourier components. By injecting these forms into Eq. 4, one obtains an eigenvalue equation for the (column) eigenvectors $F_{:b}$ and eigenvalues q_b

$$H_F F_{:b} = Q F_{:b} \quad (8)$$

with H_F called the Floquet Hamiltonian defined by:

$$\langle an | H_F | bm \rangle = H_{ab}^{n-m} + n\Omega \delta_{ab} \delta_{nm}. \quad (9)$$

This infinite Floquet Hamiltonian for our case (only $\omega_2(t)$ modulated as in Eq. 3) has the following form:

$$H_F = \begin{bmatrix} \ddots & \cdots & \cdots & \cdots & \cdots & \cdots & \cdots & \ddots \\ \vdots & \omega_1 - \Omega & \kappa & 0 & 0 & 0 & 0 & \vdots \\ \vdots & \kappa & \omega_2 - \Omega & 0 & \delta/2 & 0 & 0 & \vdots \\ \vdots & 0 & 0 & \omega_1 & \kappa & 0 & 0 & \vdots \\ \vdots & 0 & \delta/2 & \kappa & \omega_2 & 0 & \delta/2 & \vdots \\ \vdots & 0 & 0 & 0 & 0 & \omega_1 + \Omega & \kappa & \vdots \\ \vdots & 0 & 0 & 0 & \delta/2 & \kappa & \omega_2 + \Omega & \vdots \\ \ddots & \cdots & \cdots & \cdots & \cdots & \cdots & \cdots & \ddots \end{bmatrix} \quad (10)$$

This time-independent matrix is ordered in a special way: the indices go through a and b before each change in n and m . In that representation, it is clear that the coupling coefficient κ is responsible for the coupling between Floquet modes 'inside' a Fourier component, while the temporal modulation (represented by δ) couples Floquet modes across Fourier components. In other words the coupling between Floquet modes takes the form of a 'cascaded' nearest neighbor transition. For example this means that in order to couple from one Floquet mode to another mode separated by 3Ω , three successive transitions need to occur. This explains why frequency comb components typically decay as they are further away from the source frequency (see example in Fig. 3).

In order to get an estimate of the Floquet eigenvalues, one truncates the time-independent matrix H_F and numerically computes its eigenvalues. An example is shown

in Fig. 2, where the solid blue lines represent four Floquet mode frequencies in the degenerate case ($\omega_1 = \omega_2$), as a function of the coupling constant κ . As mentioned, the red dashed lines represent the static eigenfrequencies of the degenerate system ($\omega_{\pm} = \omega_1 \pm \kappa$). The Floquet frequencies form a band structure and can exhibit anti-crossings, leading to bandgap-like features. The modulation amplitude δ is the parameter responsible for the anti-crossing size: a larger δ yields a wider anti-crossing.

IV. SELECTIVE FREQUENCY CONVERSION

In this central section we examine the structure of the generated frequency combs, and discuss the relevant shaping parameters for interesting cases. Fig. 3 shows a typical comb produced by the coupled cavities, with the frequency components separated by the modulation frequency Ω . Furthermore, the sideband amplitudes decrease rapidly further away from the excitation frequency ω_0 , as the conversion is a cascade process (see e.g. the infinite Floquet matrix of Eq. 10). In this work we mainly focus on the left and right immediate sidebands ($\omega_0 \pm \Omega$), as they are expected to yield a better conversion efficiency, but some of the results can be generalized to other frequency components as well.

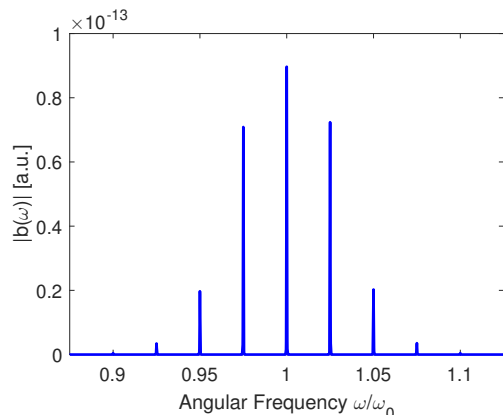


FIG. 3. Typical frequency comb produced by a time-modulated two-cavity setup. Here $\omega_1 = \omega_2$ and only the bright cavity is modulated. The parameters are such that no particular enhancement is achieved ($\omega_0 = \omega_{1,2} = 2\pi \times 10^{12}$ rad/s, $\Omega = \omega_0/40$, $\kappa = \Omega/2$, $\delta = \Omega/4$ and $\gamma = 2 \times 10^{11}$ rad/s).

The reason why the Floquet modes are so useful here is that the conversion efficiency is much more efficient when we excite a Floquet mode. This holds both for the excitation frequency ω_0 , and for the ‘destination’ frequencies $\omega_0 \pm \Omega$ (one statement leads to the other as the modes are spaced Ω apart). This means that if we excite a combination of κ and ω_0 values directly on a Floquet branch (so a point on the blue lines in Fig. 2), we are bound to have strong interactions between the components.

This intuition leads to two important cases, which we discuss in detail in the following subsections. The first

case corresponds with a κ value around the first anti-crossing ($\kappa \approx \Omega/2$) and when ω_0 is equal to a Floquet mode frequency. This leads to ‘transitions’ indicated by the four arrows at $\kappa \approx \Omega/2$ in Fig. 2 (from ω_0 to $\omega_0 \pm \Omega$). Each of these arrows corresponds to a frequency conversion from a Floquet mode to another Floquet mode. We call this case (around $\kappa \approx \Omega/2$) the ‘asymmetric conversion’ case, as it will be efficient in one direction only, leading to a single large sideband.

The second case (or regime) corresponds with a κ value around the first band crossing ($\kappa \approx \Omega$), and when ω_0 is equal to a Floquet mode frequency. The transitions of interest here are represented by the two arrows in Fig. 2 around $\kappa \approx \Omega$. This is the ‘symmetric conversion’ case, as both sidebands (at $\omega_0 \pm \Omega$) will be generated efficiently.

Furthermore, one expects that the coupling of the source to Floquet modes close to the static modes of the system will be more efficient. This is because the other Floquet harmonics are introduced in the system only via the time perturbation, whereas the two 0-order Floquet modes are connected to the static modes of the system (see numbers in Fig. 2 for the mode orders). In the end we typically observe a lower conversion efficiency for transitions that originate from (or transition to) higher order Floquet modes.

A. Asymmetric conversion

The first interesting case is the asymmetric one, as in extreme cases it leads to a highly selective conversion, where the excitation is efficiently converted towards a single new frequency. Interestingly, we will show that this is most effective at the first bandgap condition (where $\kappa = \Omega/2$). For simplicity we here discuss the degenerate case where $\omega_1 = \omega_2$.

In order to characterize the conversion efficiency, we calculate two figures of merit (FOMs) $\Gamma_{\pm} = \frac{\gamma |b(\omega_0 \pm \Omega)|}{|s(\omega_0)|}$, which indicate the fraction of excitation converted to the two direct sidebands. Here $b(\omega)$ and $s(\omega)$ are the Fourier components of the bright mode amplitude $b(t)$ and gaussian source $s(t)$, respectively. This FOM is the ratio of mode amplitudes converted from the source to a different frequency component. This fraction is useful to establish the conversion efficiency inside the coupled mode system. Note that the decay rate γ affects the FOMs. However, for relatively small values of γ (as in this paper) the FOM is proportional to γ . In contrast, too large values lead to a decrease of the FOM, as light is outcoupled too fast for intercavity interference and conversion to operate. This trade-off is also discussed in²⁸.

Fig. 4 shows the FOMs Γ_{\pm} as a function of ω_0 at the anti-crossing ($\kappa = \Omega/2$). In detail, this means we monitor Γ_{\pm} along a vertical line ($\kappa = \Omega/2$) in Fig. 2. The increased efficiency for four ω_0 values (four peaks for both Γ_+ and Γ_-) is due to the presence of the Floquet modes: the excitation ω_0 sweep cuts through four Floquet branches in this range.

In addition, there is a strong dependence concerning the direction of the transition in Fig. 4: Γ_+ is large for the two low-frequency peaks, and small for the two high-frequency peaks (and vice versa for Γ_-). This can be understood from Fig. 2: The two strong up-conversion peaks (Γ_+ is up-conversion) correspond to the blue and black arrows, leading to transitions with 0-order modes involved. The two weak up-conversion peaks at high frequencies actually mean transitions that go upwards beyond the data in Fig. 4, so concerning higher order modes as destination. Similarly, the two large down-conversion peaks (Γ_- , so red in Fig. 4) correspond to the green and red arrows in Fig. 2. Clearly, the coupling of the source to higher order modes is less efficient since these modes only exist because of the perturbation introduced by the time dependence.

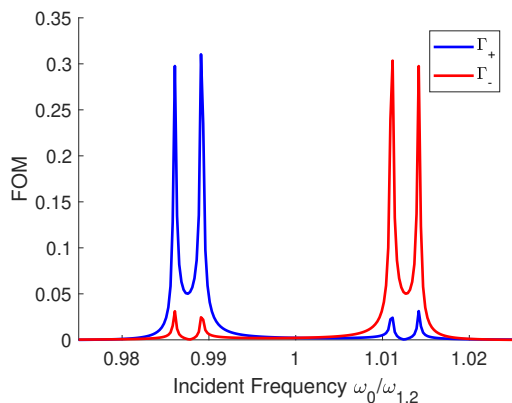


FIG. 4. Figures of merit Γ_{\pm} as a function of the incident frequency ω_0 . The frequency conversion is asymmetric at the anti-crossing (when $\kappa = \Omega/2$). When ω_0 is equal to a Floquet mode frequency, the conversion efficiency is enhanced. The difference in conversion efficiency depends on the initial and final mode order: the coupling between source and Floquet modes is better for lower order modes.

The frequency conversion is indeed highly asymmetric and selective in this case, see the example in Fig. 5, with the comb for parameters corresponding to the second peak in Fig. 4 ($\omega_0 = 0.9891 \omega_{1,2}$). The light is efficiently converted to the upper frequency sideband, with few energy in the lower sideband.

Thus, Floquet modes play an important role in the conversion process: when the incident frequency ω_0 matches a Floquet mode frequency, the conversion process is enhanced. Now we describe ways of improving the conversion efficiency when the incident frequency is on a Floquet branch. In this way, we try to exploit the Floquet mode band structure.

To find where the conversion process is most efficient, we monitor the FOMs for a few transitions of interest (see arrows in Fig. 2). In detail, we move the incident frequency *along* a Floquet band by changing the coupling coefficient κ , and we plot the corresponding FOMs in Fig. 6. This means that we follow the blue lines in

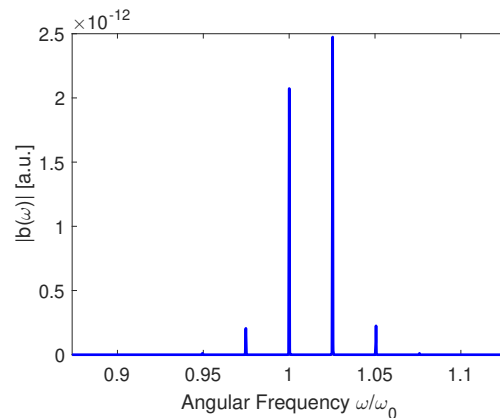


FIG. 5. Comb produced by a set of parameters corresponding to the second peak of Fig. 4 ($\omega_0 = 0.9890 \omega_{1,2}$). The conversion to the upper sideband ($\omega_0 + \Omega$) is more efficient than the conversion to the lower sideband ($\omega_0 - \Omega$) and as a result the comb is asymmetric.

Fig.2 (mainly around $\kappa = \Omega/2$), so for Fig. 6 the incident frequency is always equal to a Floquet frequency. The main trend is that all four transitions have a maximum around $\kappa = \Omega/2$: clearly the conversion is most efficient when one operates at the edge of the anti-crossing. Furthermore, one observes that the blue and red transitions are always somewhat stronger than the green and black transitions. This reflects their different mode order combinations (see the corresponding arrows in Fig. 2): the blue/red transitions start from modes closest to the center frequency ($\omega_{1,2}$), and arrive at modes away from the center. For the green/black transitions this is inverted, leading to a less efficient process.

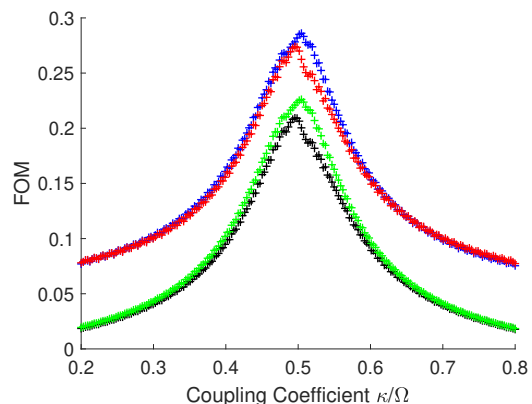


FIG. 6. Figures of merit Γ_{\pm} for the four transitions highlighted in Fig. 2 around the bandgap. The conversion efficiency is greater when the incident mode is a 0-order mode and at the band edge (for $\kappa = \Omega/2$).

B. Symmetric conversion

Another useful regime in the two-cavity system leads to a ‘symmetric’ frequency conversion, where the two first sidebands are favored and have a similar amplitude. This type of frequency conversion occurs efficiently at the first band crossing (around $\kappa \approx \Omega$), see the arrows in Fig. 2.

The up- and down-conversion FOMs (Γ_{\pm}) are shown in Fig. 7, so we follow a vertical line in Fig. 2, around the central frequency. When ω_0 is equal to the Floquet mode frequency (in this degenerate case the modes cross), the conversion efficiency is strongly enhanced (a strong peak for both FOMs). The conversion is quite symmetric, as $\Gamma_+ \approx \Gamma_-$. Due to the perturbation introduced by the time-modulation, the bands bend and do not cross exactly at $\kappa = \Omega$, but slightly before. The perturbation analysis of Section VI gives a good estimate of the correct κ value that we use in Fig. 7 ($\kappa = 0.9948 \Omega$).

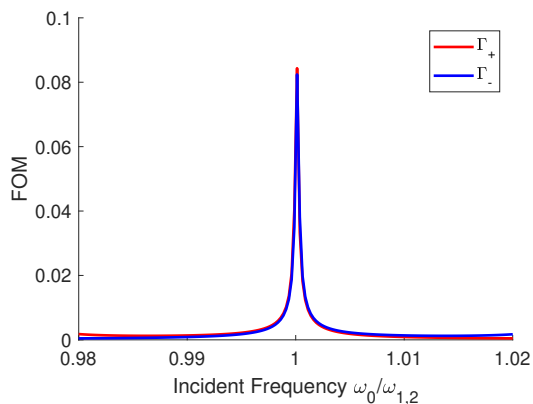


FIG. 7. Figures of merit Γ_{\pm} as a function of the incident frequency ω_0 . In this case, $\delta = \Omega/4$ and $\omega_1 = \omega_2$. At the first band crossing ($\kappa \approx \Omega$), the frequency conversion is efficient and symmetric.

Fig. 8 shows a comb produced by the parameters corresponding to the central peak of Fig. 7. Conversion to both sidebands is enhanced, as the two sidebands correspond to Floquet mode frequencies (see band diagram of Fig. 2 at $\kappa \approx \Omega$). In this case, the incident frequency corresponds to a first-order mode while the two sidebands are zeroth order.

C. Non-degenerate case

In the above discussions we presented the degenerate case where $\omega_1 = \omega_2$. Here we briefly discuss the non-degenerate case to show that the same general conclusions apply. Firstly, the band structure is similar, which we can compare in Fig. 9: the solid line is the degenerate situation, the dashed line is non-degenerate. Clearly, in the non-degenerate case, the Floquet bands no longer cross at $\kappa = 0$ as they did in the degenerate case, as the

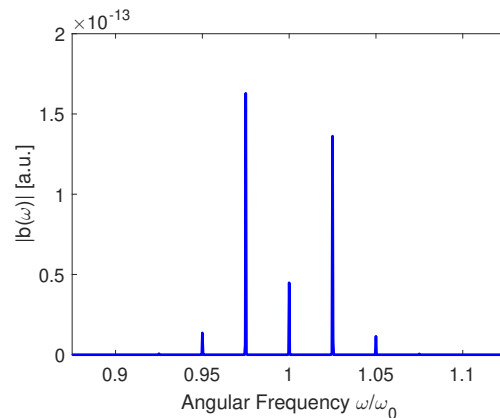


FIG. 8. Comb produced by a set of parameters corresponding to the central peak of Fig. 7. The conversion to the upper sideband ($\omega_0 + \Omega$) is nearly as efficient as the conversion to the lower sideband ($\omega_0 - \Omega$).

two cavities now have different resonance frequencies.

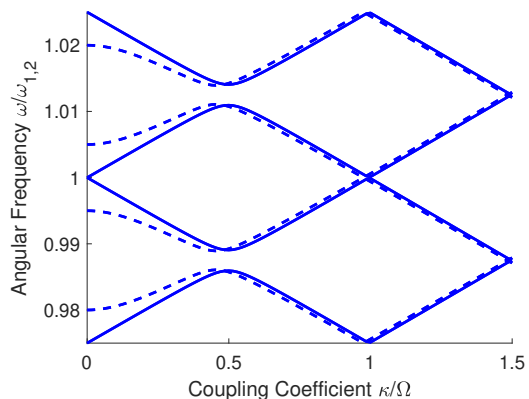


FIG. 9. Solid blue lines: Floquet modes of the system for the degenerate case (same as in Fig. 2). Dashed blue lines: non-degenerate case ($\omega_1 \neq \omega_2$). We chose these two frequencies such that $\omega_1 - \omega_2 = 2\Omega/5$.

We then consider the FOMs in the case where $\omega_1 \neq \omega_2$ around the first anti-crossing ($\kappa = \Omega/2$), see Fig. 10, in order to compare it with the degenerate case (Section IV A, Fig. 4). Note that in the non-degenerate case, the Floquet bands are slightly shifted towards smaller κ values (compare solid and dashed lines in Fig. 9). Here as well the conversion efficiency is improved when the source frequency is equal to a Floquet mode. The exact efficiency is different than in the degenerate case (Fig. 4), because of the slight difference in resonance frequencies. We will see in the next section that this can be predicted by a simple model.

We also computed the FOMs for the symmetric regime ($\kappa \approx \Omega$) in the non-degenerate case, see Fig. 11. Whereas in the degenerate case the two FOM peaks Γ_{\pm} are maximal at the same frequency (Fig. 7), here a small gap

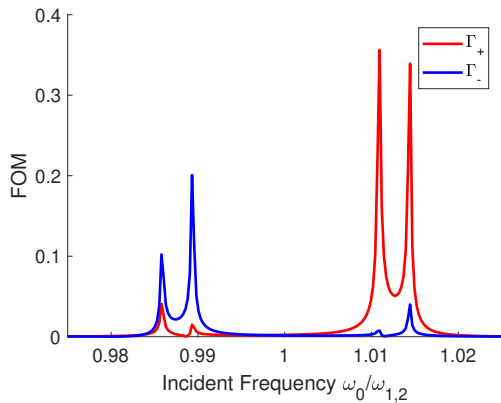


FIG. 10. Figures of merit Γ_{\pm} as a function of the incident frequency ω_0 . In this case, $\delta = \Omega$, $\omega_2 - \omega_1 = 2\Omega/5$ and $\kappa = \Omega/2$ (around the anti-crossing).

appears, meaning that the two Floquet modes do not have the same frequency, hence the peak position difference in Fig. 11. This difference is not simply due to the slight shift of the band structure seen in Fig. 9, here an anti-crossing opens whereas the two non-degenerate bands cross.

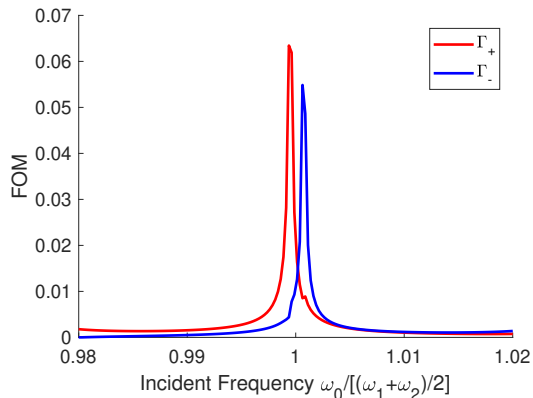


FIG. 11. Figures of merit Γ_{\pm} as a function of the incident frequency ω_0 . In this case, $\delta = \Omega$, $\omega_1 - \omega_2 = 2\Omega/5$ and $\kappa \approx \Omega$ (around the second anti-crossing).

V. THREE-FREQUENCY MODEL

In order to find the correct system parameters that enable selective frequency conversion, we can use a simplified model, where we only consider three frequencies for the two cavity mode amplitudes $a(\omega)$ and $b(\omega)$: at the source frequency ω_0 and at the two sidebands $(\omega_0 - \Omega)$ and $(\omega_0 + \Omega)$. In detail, we consider solutions of the form $f(\omega) = f_- \delta[\omega - (\omega_0 - \Omega)] + f_0 \delta[\omega - \omega_0] + f_+ \delta[\omega - (\omega_0 + \Omega)]$, where f represents the two mode amplitudes a and b . With these assumptions the CMT

Eqs. 1-3 become:

$$i(\omega_0 - \Omega)a_- = i\omega_1 a_- + i\kappa b_- \quad (11)$$

$$i\omega_0 a_0 = i\omega_1 a_0 + i\kappa b_0 + s_0 \quad (12)$$

$$i(\omega_0 + \Omega)a_+ = i\omega_1 a_+ + i\kappa b_+ \quad (13)$$

$$i(\omega_0 - \Omega)b_- = i\omega_2 b_- + \frac{\delta}{2}b_0 - \gamma b_- + i\kappa a_- \quad (14)$$

$$i\omega_0 b_0 = i\omega_2 b_0 + \frac{\delta}{2}b_- + \frac{\delta}{2}b_+ - \gamma b_0 + i\kappa a_0 \quad (15)$$

$$i(\omega_0 + \Omega)b_+ = i\omega_2 b_+ + \frac{\delta}{2}b_0 - \gamma b_+ + i\kappa a_+ \quad (16)$$

As seen in Eqs. 11-16, the coupling coefficient κ accounts for the coupling between dark and bright mode at the same frequency, while the modulation amplitude δ accounts for the coupling between the different frequency components of the bright mode b . Note that this equation system actually corresponds to the 6×6 central part of the Floquet matrix of Eq. 10. This model has the advantage of being an algebraic system, whereas the previous results were obtained through the numerical resolution of the differential equation system of Eqs. 1 and 2. It can be used to rapidly explore various situations, for example the non-degenerate case. However, since we only take into account three frequency components per mode, this model is an approximation, but it can lead to quantitatively correct results, especially in our selective cases.

We compare the results of this simple model with the numerical resolution of Eqs. 1 and 2 for two specific cases. The first case is symmetric around ω_0 , so we impose $b_- = b_+$ in Eqs. 11-16. A set of parameters found with that constraint is $\kappa = \Omega$, $\delta = \Omega/4$ and $\omega_0 = \omega_1 = \omega_2$. This specific case is represented in Fig. 12(a). In the second case, the parameters are chosen such that the conversion to the lower frequency sideband is maximized. Parameters can be found by imposing $b_0 = b_+ = 0$ in Eqs. 11-16, giving for example $\kappa = \Omega/2$, $\omega_1 = \omega_0 - \kappa$, $\delta = \Omega/4$. The results for this second set of parameters are represented in Fig. 12(b). In both cases a satisfactory agreement is found, taking the simplicity of the model into account.

This simple model allows for a more systematic approach in tuning the output spectrum: one can impose constraints in Eqs. 11-16, and solve for the system parameters that will give a desired response (as we did for Fig. 12). It also allows to understand the interference effects between the frequency components, as in some cases terms in Eqs. 11-16 cancel out, giving a single frequency output, as in Fig. 12(b). Moreover it is a useful analytic alternative to the numerical resolution of the CMT equations.

VI. TWO-LEVEL PERTURBATION

To obtain an analytical expression for the Floquet bands we can use a two-level perturbation theory⁴²⁻⁴⁴.

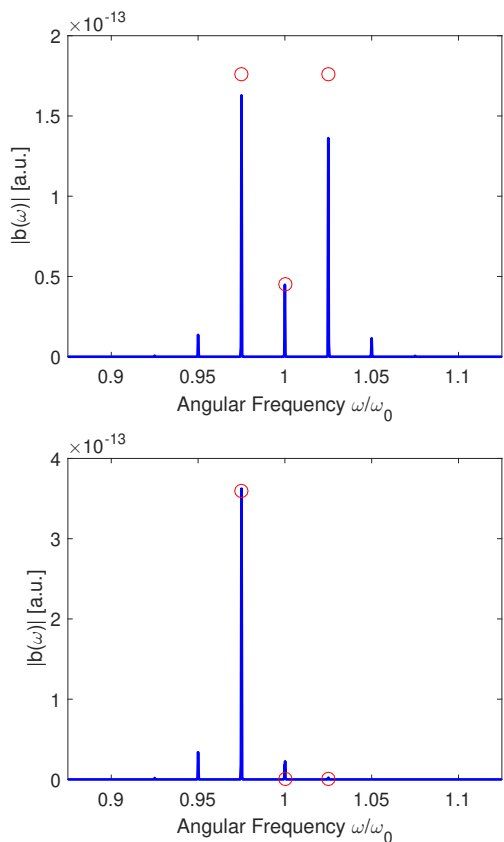


FIG. 12. Red circles are the results of the three-frequency model while the blue line is the full numerical solution. In (a) we imposed the constraint $b_- = b_+$ so the comb generated is perfectly symmetric. In (b) we imposed the constraint $b_0 = b_+ = 0$, so the frequency conversion is asymmetric.

This is useful to obtain a simple expression for the Floquet bands, so one knows which frequencies are bound to provide a good potential conversion. For simplicity we only discuss the degenerate case.

We approximate the initial Floquet Hamiltonian by a 2×2 Hamiltonian, where the contribution of the other Floquet modes is treated as a perturbation⁴⁴. To do so, we separate the Floquet Hamiltonian of Eq. 10 into a static matrix H_0 and a perturbation matrix V containing only δ terms. We apply a transformation to H_0 and V so that H_0 is diagonal and write out the eigenvalue equation component by component. Then we solve for the eigenvector components and find that they are the solution of an implicit equation involving the sum of the eigenvector components. We identify two large terms (corresponding to the crossing of static modes) and separate them from the rest of the sum. Then by iteration and by considering the first order of the perturbation, we find the two resonance frequencies of the nearly degenerate states. As seen in Fig. 2, the unperturbed bands $\omega_{1,2} + \kappa$ and $\omega_{1,2} + \Omega - \kappa$ cross at $\kappa = \Omega/2$, and open an anti-crossing in the Floquet bands. We choose these bands as the two unperturbed states for the perturbation analysis. After a

few manipulations, the perturbed Hamiltonian becomes:

$$H_2 = \begin{bmatrix} \omega_{1,2} + \Omega - \kappa + \Delta(\kappa) & \delta/4 \\ \delta/4 & \omega_{1,2} + \kappa - \Delta(\kappa) \end{bmatrix} \quad (17)$$

where $\Delta(\kappa) = \frac{\delta^2}{16(2\kappa + \Omega)}$ is the correction to the ‘static’ levels induced by the time modulation. The eigenvalues of H_2 are approximations of the Floquet mode frequencies, and are given by:

$$\omega_{\pm} = \omega_{1,2} + \frac{\Omega}{2} \pm \frac{\sqrt{\delta^4 + 64\delta^2\kappa(\Omega + 2\kappa) + 64(\Omega^2 - 4\kappa^2)^2}}{16(2\kappa + \Omega)} \quad (18)$$

Since the potential has a periodicity Ω , it is possible to completely describe all the eigenvalues of the infinite Floquet Hamiltonian with the two eigenvalues of H_2 , by adding multiples of the modulation frequency Ω . In Fig. 13 we compare the numerical eigenvalues of the Floquet matrix to the perturbation theory results. We obtain a very good agreement between the numerical eigenvalues (truncated Eq. 10) and the analytical eigenvalues obtained via perturbation theory (Eq. 18).

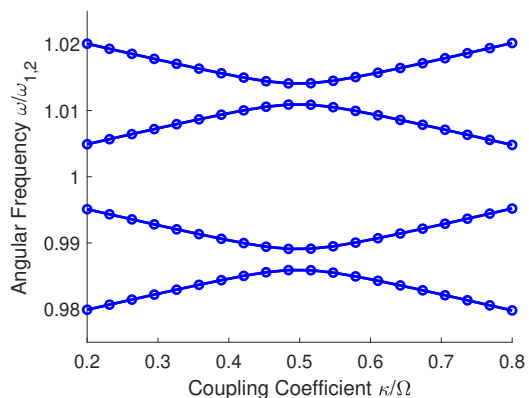


FIG. 13. Solid lines: Numerical results for the eigenvalues of the Floquet matrix. Circles: Eq. 18 and with Ω offset. The parameters used are the same as in Fig. 2.

Furthermore, this perturbation analysis allows us to find an analytical approximation for the coupling coefficient κ_c , where the Floquet modes cross for the first time (around $\kappa = \Omega$). By imposing that the two eigenvalues ω_{\pm} of Eq. 18 must be equal and solving for κ , we find (after neglecting δ^2 terms):

$$\kappa_c = \frac{\Omega}{4} \left(1 + 3\sqrt{1 - \frac{2\delta^2}{9\Omega^2}} \right) \quad (19)$$

From this expression, we see that without perturbation the bands indeed cross at $\kappa = \Omega$ as expected (see Fig. 2). This is why we employed $\kappa \approx \Omega$ for the band crossing in the previous sections.

VII. CONCLUSION

An efficient and tailored frequency conversion can be achieved with a system of coupled time-modulated cavities. We describe this process using the CMT equations adapted to time-dependent resonance frequencies. The system supports Floquet modes, arising from the time periodicity, which play an important role in the conversion efficiency. Furthermore, their band-like structure is a key element, as the conversion is enhanced in the neighbourhood of (anti-)crossings.

We exploit the coupled-cavity setup to achieve both symmetric and asymmetric frequency conversion, using the important link of these two processes with the Floquet modes. We employ perturbation theory to find an analytic approximation of the Floquet bands. Further-

more, we show how to find useful system parameters for selective frequency conversion using a straightforward three-frequency model.

This frequency conversion mechanism is fairly general, since it only requires two coupled, time-modulated resonances, such as recently demonstrated in⁴⁵. It can thus be applied to a wide range of physical systems, ranging from photonics to acoustics for example.

ACKNOWLEDGMENT

This work was supported by the Fonds pour la Formation à la Recherche dans l'Industrie et dans l'Agriculture (FRIA) and by the Fonds National de Recherche Scientifique (FNRS) in Belgium. We thank Alejandro Rodriguez for useful discussions.

-
- * Email to: Galaad.AltaresMenendez@umons.ac.be
- ¹ Y. Hadad, D. L. Sounas, and A. Alú, *Phys. Rev. B* **92**, 100304(R) (2015).
 - ² D. L. Sounas and A. Alú, *Nat. Photonics* **11**, 774 (2017).
 - ³ Z. Yu and S. Fan, *Nat. Photonics* **3**, 91 (2009).
 - ⁴ H. Lira, Z. Yu, S. Fan, and M. Lipson, *Phys. Rev. Lett.* **109**, 033901 (2012).
 - ⁵ R. Fleury, D. L. Sounas, C. F. Sieck, M. R. Haberman, and A. Alú, *Science* **343**, 516 (2014).
 - ⁶ D. Correas-Serrano, J. S. Gomez-Diaz, D. L. Sounas, Y. Hadad, A. Alvarez-Melcon, and A. Alú, *IEEE Antennas Wirel. Propag. Lett* **15**, 1529 (2016).
 - ⁷ E. J. Reed, M. Soljačić, and J. D. Joannopoulos, *Phys. Rev. Lett.* **91**, 133901 (2003).
 - ⁸ M. Notomi and S. Mitsugi, *Phys. Rev. A* **73**, 051803(R) (2006).
 - ⁹ T. Kampfrath, D. M. Beggs, T. P. White, A. Melloni, T. F. Krauss, and L. Kuipers, *Phys. Rev. A* **81**, 043837 (2010).
 - ¹⁰ D. M. Beggs, T. F. Krauss, L. Kuipers, and T. Kampfrath, *Phys. Rev. Lett.* **108**, 033902 (2012).
 - ¹¹ K. Fang, Z. Yu, and S. Fan, *Nat. Photonics* **6**, 782 (2012).
 - ¹² K. Fang, Z. Yu, and S. Fan, *Phys. Rev. Lett.* **108**, 153901 (2012).
 - ¹³ A. B. Khanikaev, S. Hossein Mousavi, W.-K. Tse, M. Kargarian, A. H. MacDonald, and G. Shvets, *Nat. Mater* **12**, 233 (2012).
 - ¹⁴ L. Lu, J. D. Joannopoulos, and M. Soljačić, *Nat. Photonics* **8**, 821 (2014).
 - ¹⁵ D. V. Else, B. Bauer, and C. Nayak, *Phys. Rev. Lett.* **117**, 090402 (2016).
 - ¹⁶ J. Zhang, P. W. Hess, A. Kyprianidis, P. Becker, A. Lee, J. Smith, G. Pagano, I.-D. Potirniche, A. C. Potter, A. Vishwanath, N. Y. Yao, and C. Monroe, *Nature* **543**, 217 (2017).
 - ¹⁷ S. Choi, J. Choi, R. Landig, G. Kucsko, H. Zhou, J. Isoya, F. Jelezko, S. Onoda, H. Sumiya, V. Khemani, C. von Keyserlingk, N. Y. Yao, E. Demler, and M. D. Lukin, *Nature* **543**, 221 (2017).
 - ¹⁸ S. F. Preble, Q. Xu, and M. Lipson, *Nat. Photonics* **1**, 293 (2007).
 - ¹⁹ M. T. Wade, X. Zeng, and M. A. Popovic, *Opt. Lett.* **40**, 107 (2015).
 - ²⁰ B. Wang, J. Teng, and X. Yuan, *Appl. Phys. Lett.* **98**, 263111 (2011).
 - ²¹ M. Jablan, H. Buljan, and M. Soljačić, *Phys. Rev. B* **80**, 245435 (2009).
 - ²² A. N. Grigorenko, M. Polini, and K. S. Novoselov, *Nat. Photonics* **6**, 749 (2012).
 - ²³ J. Chen, M. Badioli, P. Alonso-González, S. Thongrattanasiri, F. Huth, J. Osmond, M. Spasenović, A. Centeno, A. Pesquera, P. Godignon, A. Zurutuza Elorza, N. Camara, F. J. García de Abajo, R. Hillenbrand, and F. H. L. Koppens, *Nature* **487**, 77 (2012).
 - ²⁴ F. J. Garcia de Abajo, *ACS Photonics* **1**, 135 (2014).
 - ²⁵ L. A. Falkovsky, *J. Phys. Conf. Ser* **129**, 012004 (2008).
 - ²⁶ F. Wang, Y. Zhang, C. Tian, C. Girit, A. Zettl, M. Crommie, and Y. R. Shen, *Science* **320**, 206 (2008).
 - ²⁷ V. Giniis, P. Tassin, T. Koschny, and C. M. Soukoulis, *Phys. Rev. B* **91**, 161403(R) (2015).
 - ²⁸ G. Altares Menendez and B. Maes, *Phys. Rev. B* **95**, 144307 (2017).
 - ²⁹ M. Minkov, Y. Shi, and S. Fan, *APL Photonics* **2**, 076101 (2017).
 - ³⁰ T. J. Kippenberg, R. Holzwarth, and S. A. Diddams, *Science* **332**, 555 (2011).
 - ³¹ P. Del'Haye, A. Schliesser, O. Arcizet, T. Wilken, R. Holzwarth, and T. J. Kippenberg, *Nature* **450**, 1214 (2007).
 - ³² H. A. Haus, *Waves and Fields in Optoelectronics* (Prentice Hall, 1983).
 - ³³ S. Fan, W. Suh, and J. D. Joannopoulos, *J. Opt. Soc. Am. A* **20**, 569 (2003).
 - ³⁴ A. Pick, Z. Lin, W. Jin, and A. W. Rodriguez, *Phys. Rev. B* **96**, 224303 (2017).
 - ³⁵ A. N. Abbas, G. Liu, B. Liu, L. Zhang, H. Liu, D. Ohlberg, W. Wu, and C. Zhou, *ACS Nano* **8**, 1538 (2014).
 - ³⁶ A. Y. Nikitin, T. Low, and L. Martin-Moreno, *Phys. Rev. B* **90**, 041407(R) (2014).
 - ³⁷ C. T. Phare, Y. Daniel Lee, J. Cardenas, and M. Lipson, *Nat. Photonics* **9**, 511 (2015).

- ³⁸ Y. Sivan and J. B. Pendry, Phys. Rev. Lett. **106**, 193902 (2011).
- ³⁹ D. K. Kalluri, *Electromagnetics of Time Varying Complex Media: Frequency and Polarization, Second Edition* (CRC Press, 2010).
- ⁴⁰ G. Altares Menendez and B. Maes, Opt. Lett. **42**, 5006 (2017).
- ⁴¹ N. Wang, Z.-Q. Zhang, and C. T. Chan, Phys. Rev. B **98**, 085142 (2018).
- ⁴² J. H. Shirley, Phys. Rev. **138**, B979 (1965).
- ⁴³ H. Salwen, Phys. Rev. **99**, 1274 (1955).
- ⁴⁴ J. H. Shirley, *Interaction of a Quantum System with a Strong Oscillating Field*, Ph.D. thesis, California Institute of Technology (1963).
- ⁴⁵ M. Zhang, C. Wang, Y. Hu, A. Shams-Ansari, T. Ren, S. Fan, and M. Lončar, Nat. Photonics **13**, 36 (2019).